Exchange-mediated magnon-phonon scattering in monolayer CrI₃

Andi Cong, Jie Liu, Weishan Xue, Huicong Liu, Yi Liu,[*] and Ka Shen[†]

The Center for Advanced Quantum Studies and Department of Physics, Beijing Normal University, Beijing 100875, China

The interplay between magnons and phonons and its influences on magnon dissipation have attracted widespread attentions. Whereas the previous theoretical works were usually restricted to the interactions between low-frequency magnons and acoustic phonons in the long-wavelength region, in the present work we go beyond this limit and investigate the magnon relaxation in a two-dimensional ferromagnet, a monolayer CrI₃, through magnon-phonon scattering channels mediated by the variation of the exchange strength resulting from all-wavelength acoustic phonons as well as the optical ones. With a precise description of the magnon and phonon Bloch states from first principles, we evaluate the magnon relaxation rate due to these exchange-mediated magnon-phonon scatterings and reveal rich features in its momentum dependence, which reflects nicely the role of the associated phonons with in-plane atomic vibrations. The magnon-number-conserving scattering is found to be orders of magnitude stronger than the magnon-number-nonconserving scattering due to the weak anisotropic exchange coupling or dipole-dipole interaction. Our first-principles-based approach provides a better solution for the quantitative evaluation of the magnon dissipation by phonons.

I. INTRODUCTION

Regarded as potential candidates for next-generation information carriers, magnons or spin waves in magnetic materials contain a precessional phase degree of freedom, which allows us to design various spin-wave-based logic gates [1–7] for computing applications [8–10] with fast processing speed, thanks to their high frequency (up to terahertz range) [11–16]. As the spin waves can propagate in magnetic insulators, the absence of Joule heating therein provides the opportunity to, as an expected advantage compared to the traditional electronic devices, remarkably reduce the energy consumption [17,18]. There is however a bottleneck for realistic spin-wave-based applications, namely the unavoidable magnetic damping in magnetic materials, which always causes a decay of the spin-wave signal coherently in the amplitude and precession phase or incoherently in the magnon number in both space and time domains. Microscopically, the magnetic damping originates from various mechanisms, such as magnetic inhomogeneity [19–24], spin-lattice interaction [25–31], spin-spin interaction [32–37], as well as the spin exchange with itinerant electrons [38–42]. Among them, the spin-lattice interaction, recognized as the intrinsic interaction, has received intensive studies in ferromagnets [43–45], ferrimagnets [46–50], and also antiferromagnets [51–53].

In the long-wavelength limit, the spin-lattice interaction can be well described by the phenomenological magnetoelastic coupling [25,26,28]. In practice, for instance in the thermal magnon transport at a relatively high temperature, one has to go beyond the long-wavelength limit, as the

relative atomic displacement can become important and activate additional contributions, such as the temporal modulation in the exchange strengths between the magnetic moments [27,29,30]. The theoretical evaluation of these contributions is quite challenging, because the spin and lattice dynamics in the short-wavelength regime is too complicated to meet the requirements for the widely adopted approximation in analytical calculation [44,45,49,51]. One useful technique to capture the thermal fluctuation is the so-called "frozen-phonon/magnon method" in first-principles calculations [54–56], where the influence of the mechanical vibrations and spin excitation is modeled by the average over a set of static randomly disordered lattice and spin configurations, determined from the thermal occupation of phonon and magnon spectra [43,47,50,53]. While this technique has been demonstrated to be sufficient for a quantitative description of the electronic spin transport [57], it is apparently not suitable to explore the dynamic and transport properties of the magnons and phonons themselves. For the latter, one option is to perform combined spin-lattice atomistic simulations [58,59], which however require very expensive computation, so that the lattice degree of freedom is usually treated statically for the spin dynamics [60,61] or vice versa. Our aim is thus to develop a first-principles approach to quantitatively investigate the spin-lattice interaction beyond the long-wavelength limit with spin and lattice treated on an equal footing.

The idea is quite straightforward. Starting from a spin-lattice coupled atomic model, we derive the analytical formalism for the magnon-phonon interaction, including both linear [62] and higher order coupling contributions. By evaluating the modeling parameters from first-principles calculation, we obtain the proper Bloch states of both magnons and phonons, not only their spectra but also the corresponding wave functions, in the entire Brillouin zone (BZ), which

---

[*]yiliu@bnu.edu.cn
[†]kashen@bnu.edu.cn

then allows us to calculate the interaction strength between magnons and phonons in the derived formalism [62]. Taking the monolayer of two-dimensional (2D) van der Waals (vdW) ferromagnet CrI_3 [63] as an example, we study the magnon-phonon scattering processes due to the aforementioned phonon-induced variation of the exchange interaction. From the explicit analysis on the contributions from different scattering channels, the essential role of the phonon modes with in-plane atomic vibrations is revealed in both magnon-number-conserving (MNC) scattering derived from the isotropic exchange interaction and the magnon-number-nonconserving (MNNC) scattering due to the anisotropy of the exchange interaction or dipole-dipole interaction.

II. MODEL AND FORMALISM

We consider an easy-axis ferromagnetic system and start with a minimal Hamiltonian containing Heisenberg-type exchange interaction and on-site magnetic anisotropy as

$$H_0 = \sum_i A_i^z (S_i^z)^2 - \frac{1}{2} \sum_{i,j} J_{ij} \mathbf{S}_i \cdot \mathbf{S}_j, \quad (1)$$

where the anisotropy coefficient $A_i^z < 0$ defines the easy axis along z direction. Assuming that the exchange constant J_{ij} depends solely on the atomic distance between magnetic ions $r_{ij} = |\mathbf{r}_i - \mathbf{r}_j|$, one can expand the exchange tensor around the equilibrium coordinates $\mathbf{R}_i$ through $\mathbf{r}_i = \mathbf{R}_i + \mathbf{X}_i$ as

$$J_{ij} \approx \bar{J}_{ij} + J'_{ij}[(\mathbf{X}_i - \mathbf{X}_j) \cdot \mathbf{d}_{ij}], \quad (2)$$

with $\mathbf{d}_{ij} = (\mathbf{R}_i - \mathbf{R}_j)/|\mathbf{R}_i - \mathbf{R}_j|$ and $J'_{ij} = \partial J_{ij}/\partial r_{ij}$ at $r_{ij}^0 = |\mathbf{R}_i - \mathbf{R}_j|$. By substituting Eq. (2) into Eq. (1), one can separately write a pure spin Hamiltonian

$$H^m = \sum_i A_i^z (S_i^z)^2 - \frac{1}{2} \sum_{i,j} \bar{J}_{ij} \mathbf{S}_i \cdot \mathbf{S}_j, \quad (3)$$

and a coupling term between spin and lattice

$$H^{mp} = -\frac{1}{2} \sum_{i,j} J'_{ij}[(\mathbf{X}_i - \mathbf{X}_j) \cdot \mathbf{d}_{ij}] \mathbf{S}_i \cdot \mathbf{S}_j. \quad (4)$$

After performing the standard procedures with Holstein-Primakoff (HP) transformation [64] to the spin operators $S_i^+ = S_i^x + iS_i^y \simeq \sqrt{2S} a_i$ and $S_i^z = S - a_i^\dagger a_i$ followed by Fourier transformation, one can calculate all magnon states in the momentum space from Eq. (3). The atomic displacement in the spin-lattice coupling can be expressed as

$$\mathbf{X}_i = N^{-\frac{1}{2}} \sum_{\mathbf{q},\sigma} \mathbf{e}_{i\mathbf{q}\sigma} X_{i\mathbf{q}\sigma} e^{i\mathbf{q}\cdot\mathbf{R}_i}, \quad (5)$$

where N is the number of unit cells and $X_{i\mathbf{q}\sigma} = \sqrt{\hbar/(2m_i\omega_{\mathbf{q}\sigma})}(c_{\mathbf{q}\sigma} + c_{-\mathbf{q}\sigma}^\dagger)$ with m_i being the mass of the ith magnetic atom. $\omega_{\mathbf{q}\sigma}$ and $c_{\mathbf{q}\sigma}$ ($c_{-\mathbf{q}\sigma}^\dagger$) represent the frequency and the annihilation (creation) operator of the σth phonon mode at wave vector $\mathbf{q}$, respectively. And $\mathbf{e}_{i\mathbf{q}\sigma}$ stands for the corresponding projection of the polarization vector on the ith magnetic atom. The phonon spectrum and polarization vectors can be carried out from a first-principles calculation [65,66].
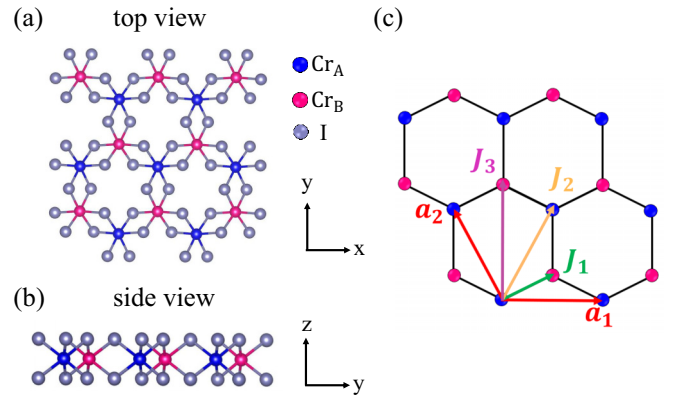
FIG. 1. (a) Top and (b) side view of the monolayer CrI_3. (c) The honeycomb lattice of the magnetic Cr^{3+} ions. The red arrows $\mathbf{a}_1$ and $\mathbf{a}_2$ are the basic translation vectors. The green, orange, and purple arrows indicate the nearest-, next-nearest-, and third-nearest-neighbor exchange pairs, whose isotropic exchange parameters are defined as J_1, J_2, and J_3, respectively.

The magnon-phonon scattering rates due to Eq. (4) can then be calculated from the Fermi's golden rule

$$W_{i\to f} \approx \frac{2\pi}{\hbar} |\langle f|H^{mp}|i\rangle|^2 \delta(E_f - E_i), \quad (6)$$

where $|i\rangle$ and $|f\rangle$ stand for the initial and final states, respectively, and E_i and E_f are the corresponding total energies. The δ function reflects the energy conservation and, for numerical calculations, is usually replaced by a Gaussian function [49]

$$\delta(E_1 - E_2) \to \frac{1}{\sqrt{\pi}\zeta} e^{-\frac{(E_1-E_2)^2}{\zeta^2}}, \quad (7)$$

with ζ being a broadening parameter. In this work we adopt $\zeta = 1$ meV, which is sufficient to achieve the convergences.

III. NUMERICAL RESULTS IN A MONOLAYER CrI_3

For explicit calculations we specify a monolayer of the ferromagnetic vdW insulator CrI_3, where the strong magnetocrystalline anisotropy protects the long-range magnetic order. As schematically shown in Fig. 1, there are two inequivalent types of Cr atoms, denoted as A and B, forming a honeycomb lattice, each surrounded by six I atoms forming a slightly warped octahedron. The spin of the magnetic Cr atoms are $S = 3/2$. J_1, J_2, and J_3 in Fig. 1(c) representing the exchange parameters between the nearest (A-B), next-nearest (A-A or B-B), and third-nearest (A-B) neighbors, which are currently assumed to be isotropic while the anisotropy in the exchange interaction will be discussed in Sec. IV.

A. Magnon spectrum

After straightforward calculation [67–69] we derive the magnon Hamiltonian as

$$H^m = \sum_k A_k(a_k^\dagger a_k + b_k^\dagger b_k) + B_k a_k^\dagger b_k + B_k^* a_k b_k^\dagger, \quad (8)$$

where

$$A_{\mathbf{k}}/S = 3J_1 + 6J_2 + 3J_3 - 2A_z$$
$$- 2J_2\left[\cos(k_x a) + 2\cos\left(\frac{k_x a}{2}\right)\cos\left(\frac{\sqrt{3}k_y a}{2}\right)\right], \quad (9)$$

$$B_{\mathbf{k}}/S = -J_1\left[e^{i\frac{\sqrt{3}k_y a}{3}} + 2\cos\left(\frac{k_x a}{2}\right)e^{-i\frac{\sqrt{3}k_y a}{6}}\right]$$
$$- J_3\left[e^{-i\frac{2\sqrt{3}k_y a}{3}} + 2\cos(k_x a)e^{i\frac{\sqrt{3}k_y a}{3}}\right], \quad (10)$$

with a being the lattice constant. $a_{\mathbf{k}}$ ($a_{\mathbf{k}}^{\dagger}$) and $b_{\mathbf{k}}$ ($b_{\mathbf{k}}^{\dagger}$) are annihilation (creation) magnon operators of A (B) sublattice for a wave vector $\mathbf{k}$, which satisfy the boson commutation rules $[a_{\mathbf{k}}, a_{\mathbf{k}'}^{\dagger}] = \delta_{\mathbf{k},\mathbf{k}'}$ and $[b_{\mathbf{k}}, b_{\mathbf{k}'}^{\dagger}] = \delta_{\mathbf{k},\mathbf{k}'}$, respectively.

By diagonalizing Eq. (8), one obtains the dispersion relations of the acoustic (denoted as $\alpha_{\mathbf{k}}$) and optical (denoted as $\beta_{\mathbf{k}}$) magnon branches

$$\omega_{\alpha_{\mathbf{k}}/\beta_{\mathbf{k}}} = A_{\mathbf{k}} \mp |B_{\mathbf{k}}|, \quad (11)$$

where "$-$" and "$+$" on the right-hand side are referred to as α and β modes, respectively, and the corresponding magnon operators of the Bloch states

$$\alpha_{\mathbf{k}}/\beta_{\mathbf{k}} = \mu_{\alpha_{\mathbf{k}}/\beta_{\mathbf{k}}}a_{\mathbf{k}} + \nu_{\alpha_{\mathbf{k}}/\beta_{\mathbf{k}}}b_{\mathbf{k}}, \quad (12)$$

with

$$\mu_{\alpha_{\mathbf{k}}/\beta_{\mathbf{k}}} = \mp\frac{B_{\mathbf{k}}^*}{\sqrt{2}|B_{\mathbf{k}}|}, \quad \nu_{\alpha_{\mathbf{k}}/\beta_{\mathbf{k}}} = \frac{1}{\sqrt{2}}. \quad (13)$$

In order to evaluate the three exchange interaction coefficients J_{1-3}, we perform first-principles calculation to compute total energy for 11 inequivalent collinear spin configurations with atomic spins flipped on different sites and then linear regressions of the total energies to extract the exchange coefficients [47,50]. Self-consistent calculations for the configurations are carried out using density functional theory implemented in the Vienna *ab initio* simulation package (VASP6) [70,71]. The Perdew-Burke-Ernzerhof (PBE) [72] functional is employed to describe the exchange and correlation. The PBE version of all-electron projector augmented wave (PAW) [73,74] potentials are adopted with the $3p^6 3d^5 4s^1$ states of Cr and $4d^{10}5s^2 5p^2$ states of I treated as valence electrons. The plane-wave basis set is truncated with a cut-off energy of 600 eV and the k points in the BZ are sampled with a $10 \times 10 \times 1$ mesh using the Monkhorst-Pack scheme [75]. The exchange parameters are obtained as

$$J_1 = 2.94 \pm 0.04 \text{ meV},$$
$$J_2 = 0.62 \pm 0.02 \text{ meV},$$
$$J_3 = -0.16 \pm 0.02 \text{ meV}, \quad (14)$$

comparable to the reported values in the literature [76–79]. All of our above calculations have been carried out without taking into account relativistic (spin-orbit) effects which have been approved to have negligible effects upon isotropic exchange interactions in Ref. [79]. A similar energy-based calculation with tilted spins gives the on-site magnetic anisotropy parameter $A_z \approx -0.364$ meV. With these exchange and anisotropy parameters, the magnon spectrum from Eq. (11) is plotted as red curves in Fig. 2(d) with a magnon gap at Γ point $\Delta \approx$
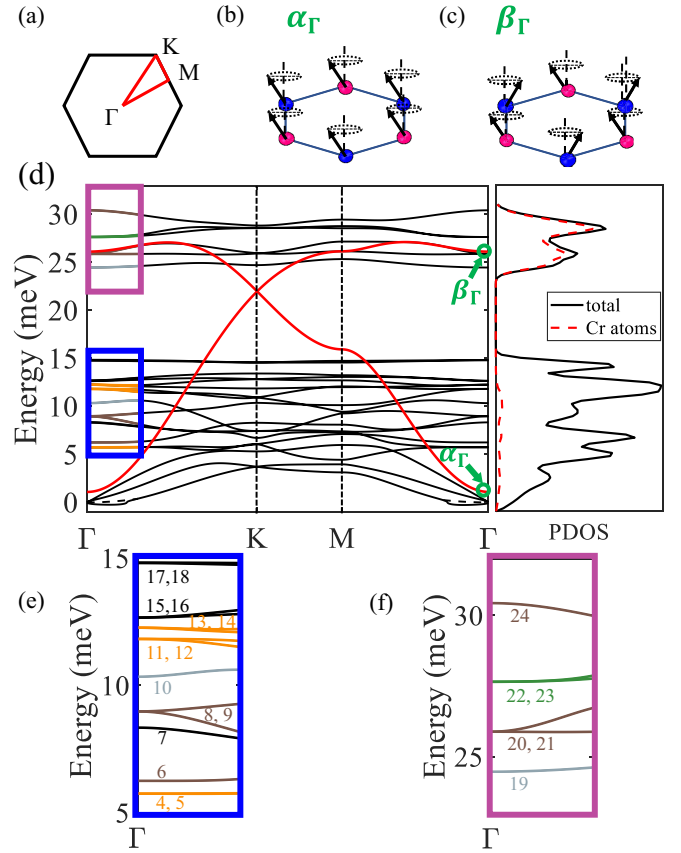
FIG. 2. (a) The BZ of CrI_3 with the red lines constructing a closed path Γ-K-M-Γ. (b) and (c) The spin precession of the acoustic and optical magnon modes at Γ point. (d) The magnon spectrum (red curves) and phonon spectrum (black curves) in the monolayer CrI_3 along the closed path Γ-K-M-Γ with the phonon density of states (PDOS) and its projection on the Cr atoms shown in the right panel. (e) and (f) Enlarged plotting of the two frequency windows in (d) with each branch indexed according to their energies, from the lowest to the highest value, and grouped by colors as explained in the main text.

1.1 meV, showing a fairly good agreement with the previous theoretical result from time-dependent density-functional perturbation theory [62] and the experimental observation [80]. The eigenfunctions, obtained meanwhile, describe the dynamics of the specific magnon modes. As illustrated in Figs. 2(b) and 2(c), around the Γ point, the acoustic (optical) magnon α_Γ (β_Γ) corresponds to in-phase (out-of-phase) precession of the two sublattices.

B. Phonon spectrum

To calculate the phonon spectra, we follow the density-functional perturbation theory approach [81,82] with the QUANTUM ESPRESSO software package [65,66]. A $4 \times 4 \times 1$ mesh is used to sample the phonon modes in the whole BZ. For each $\mathbf{k}$ point we obtain the frequencies as well as the polarization vectors that describe the directions of the oscillation of each atom. The phonon energies are plotted as black curves in Fig. 2(d) together with the magnon modes (in red). It is worth mentioning that there are imaginary

frequencies for the lowest acoustic branch within the range of less than 8% of BZ around Γ point, as found with many other 2D materials [83–85], though our calculations are well converged and the lattice structure has been completely relaxed (the residual interatomic forces are below 0.01 eV/Å). To correct this artificial effect and avoid unphysical consequence in magnon-phonon scattering calculations, we adopt the analytical solution $E_{q,1}^{\mathrm{ph}} \sim q^2$, which is expected for layer bending (or ripple) modes in 2D materials [86,87], for the lowest acoustic phonon mode in this small area, as shown by the dashed curve. Interestingly, the imaginary frequency problem was fixed in a similar phonon calculation reported in Ref. [62], which might be due to the calculation details there, such as the choices of pseudopotentials or other parameters. A recent paper showed that a proper acoustic sum rule might also help us to solve the imaginary frequency problem in the 2D phonon calculation and recover the quadratic dispersion of the bending mode [88]. The projected density of states of phonons (PDOS) in the right panel of Fig. 2(d) show that the high frequency is mainly contributed by the Cr atoms because of their smaller mass than that of the I atoms.

The magnon and phonon spectra overlap with each other, providing vast opportunities for magnon-phonon scattering. Lattice oscillations described by phonon modes give rise to changes in distances between Cr atoms, which in turn affect the exchange interaction. In the following we focus on the spatial displacements of the Cr atoms by assuming that the exchange parameters are only negligibly affected by the shift of the I atoms (although the latter can in principle be taken into account in our formalism but that requires explicit treatment of the indirect exchange interaction). Taking Γ point as an example, we analyze the changes of distances between Cr atoms due to phonons. We have 24 phonon branches in total. Besides the acoustic branches, there are 15 branches in the low energy window (blue window) and 6 branches in the high energy range (purple window), as shown in Figs. 2(e) and 2(f), respectively.

By carefully checking the polarization vectors $\mathbf{e}_{i\Gamma\sigma}$ of these modes, we find: (i) Branches 7 and 15–18 (black ones) contain only the motions of I atoms as shown in Fig. 2(d). (ii) Branches 9 and 20, 8 and 21, and 6 and 24 (brown ones) lead to Cr atoms at A and B sublattices vibrating with the same amplitude in the directions of x, y, and z, respectively. (iii) Branches 10 and 19 (gray ones) result in opposite motion of the two Cr sublattices along z direction. All these modes yield negligible changes in the bond length and thus the exchange interactions between Cr atoms. This can be seen from the rather small amplitude in the left panel of Fig. 3(a), where we take branches 19 and 20, belonging to (iii) and (ii), respectively, as examples. The time evolution of the atomic distances between nearest Cr_A and Cr_B is calculated as

$$\sqrt{N}\delta R_{ij,\sigma}(t) = |\sqrt{N}\mathbf{X}_{A\Gamma\sigma} - \sqrt{N}\mathbf{X}_{B\Gamma\sigma}|\cos(\omega_{\Gamma\sigma}t). \quad (15)$$

As a contrast, the vibrations of Cr_A and Cr_B from branches 5, 11, and 14 (opposite along y direction) as shown in Fig. 3(b), vibrations from branches 4, 12, and 13 (opposite along x direction) as shown in Fig. 3(c), and those from branches 22 (opposite along x direction) and 23 (opposite along y direction) as shown in Fig. 3(d), lead to significant modification
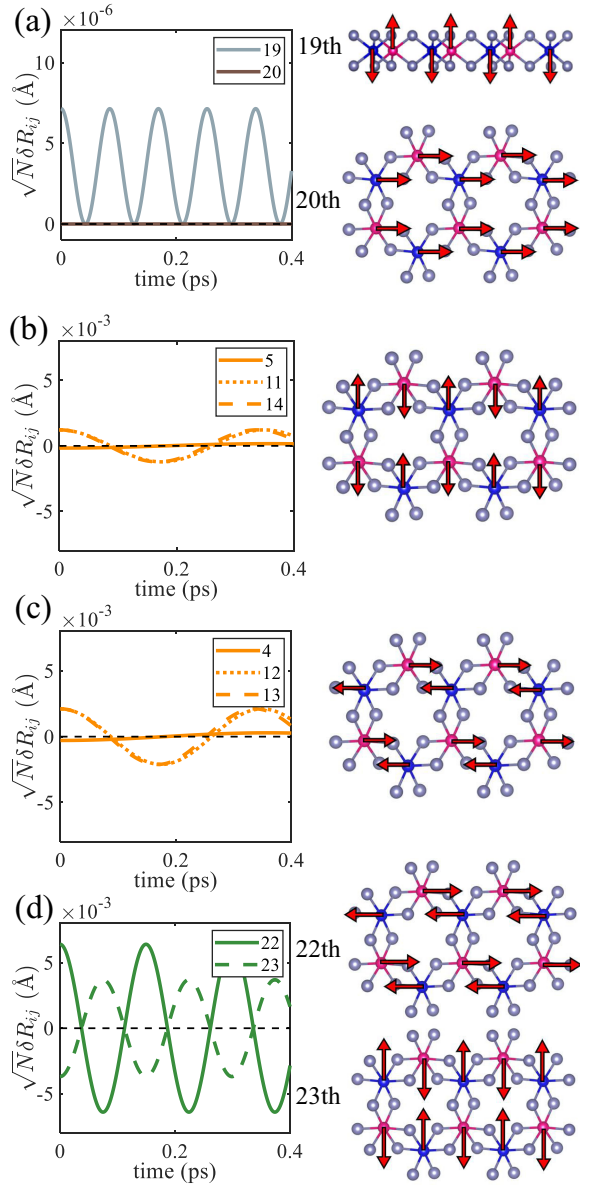
FIG. 3. The evolution of the distance (left panel) between neighboring Cr_A and Cr_B and the illustration of the dynamics of the magnetic atoms (right panel) for the typical phonon modes around Γ point.

in the Cr-Cr distance. It is worth mentioning that, though the PDOS, as shown in Fig. 2(d), for branches 5, 11, and 14 and branches 4, 12, and 13, are much smaller than those for branches 22 and 23, important influences on magnon-phonon scattering from branches 4, 5, and 11–14 are found, as shown in the next section.

C. MNC magnon-phonon scatterings

We further write out the atomic displacement given in Eq. (5) into the present two-sublattice system as

$$\mathbf{X}_{iA(B)} = N^{-\frac{1}{2}}\sum_{q,\sigma} \mathbf{e}_{A(B)q\sigma}X_{q\sigma}e^{iq\cdot\mathbf{R}_{iA(B)}}, \quad (16)$$

where $X_{q\sigma} = \sqrt{\hbar/(2m_{\mathrm{Cr}}\omega_{q\sigma})}(c_{q\sigma} + c_{-q\sigma}^{\dagger})$. By applying Eqs. (12) and (16), the magnon-phonon interaction Hamiltonian (4) can be expressed as

$$H_{\mathrm{c}}^{\mathrm{mp}} = \frac{1}{\sqrt{N}} \sum_{q,k,\sigma} \left[\Theta_{k,k-q,\sigma}^{\mathrm{c},\alpha\alpha} \alpha_{k}^{\dagger}\alpha_{k-q} + \Theta_{k,k-q,\sigma}^{\mathrm{c},\beta\beta} \beta_{k}^{\dagger}\beta_{k-q} \right.$$
$$\left. - \Theta_{k,k-q,\sigma}^{\mathrm{c},\alpha\beta} \alpha_{k}^{\dagger}\beta_{k-q} - \Theta_{k,k-q,\sigma}^{\mathrm{c},\beta\alpha} \beta_{k}^{\dagger}\alpha_{k-q} \right] X_{q\sigma}, \quad (17)$$

where the sum runs over all momenta q and k in the BZ and the coupling coefficients are defined as

$$\Theta_{k,k',\sigma}^{\mathrm{c},\kappa_1\kappa_2} = \frac{S}{(\nu_{\beta_k}^{*}\mu_{\alpha_k}^{*} - \nu_{\alpha_k}^{*}\mu_{\beta_k}^{*})(\nu_{\beta_{k'}}\mu_{\alpha_{k'}} - \nu_{\alpha_{k'}}\mu_{\beta_{k'}})}$$
$$\times \left\{ \sum_{\langle i,j \rangle, \langle\langle\langle i,j \rangle\rangle\rangle} J_{ij}' \left[h_{1,k}^{*}h_{2,k'}e^{-ik'\cdot R_{ij}} + h_{1,k}^{*}\gamma_{2,k'} \right. \right.$$
$$\left. + \gamma_{1,k}^{*}\gamma_{2,k'}e^{-ik\cdot R_{ij}} + \gamma_{1,k}^{*}h_{2,k'}e^{-i(k+k')\cdot R_{ij}} \right]$$
$$\times \left(e_{\mathrm{B},k-k'\sigma}^{ij} e^{ik\cdot R_{ij}} - e_{\mathrm{A},k-k'\sigma}^{ij} e^{ik'\cdot R_{ij}} \right)$$
$$+ \sum_{\langle\langle i,j \rangle\rangle} iJ_{ij}' \left(h_{1,k}^{*}h_{2,k'} e_{\mathrm{A},k-k'\sigma}^{ij} + \gamma_{1,k}^{*}\gamma_{2,k'} e_{\mathrm{B},k-k'\sigma}^{ij} \right)$$
$$\left. \times \left[\sin((k'-k)\cdot R_{ij}) + \sin(k\cdot R_{ij}) - \sin(k'\cdot R_{ij}) \right] \right\},$$
$$(18)$$

in which

$$\gamma_{1(2),k} = \mu_{\beta_k}, \quad h_{1(2),k} = \nu_{\beta_k}, \quad \text{if } \kappa_{1(2)} = \alpha,$$
$$\gamma_{1(2),k} = \mu_{\alpha_k}, \quad h_{1(2),k} = \nu_{\alpha_k}, \quad \text{if } \kappa_{1(2)} = \beta, \quad (19)$$

and $e_{\mathrm{A(B)},q\sigma}^{ij} = d_{ij} \cdot e_{\mathrm{A(B)}q\sigma}$. The superscript "c" indicates that the magnon number is conserved during the scattering process given by Eq. (17), guaranteed by the spin conservation in the isotropic exchange Hamiltonian. The numerical evaluation of the parameters J_{1-3}' gives

$$J_1' \approx 1.483\,\mathrm{meV/Å}, \quad J_2' \approx -0.460\,\mathrm{meV/Å},$$
$$J_3' \approx 0.404\,\mathrm{meV/Å},$$

which are comparable with those reported in previous works [79,89]. The technical details and more discussions on this calculation can be found in Appendix A.

Specifically, for the scattering process with an initial η_k magnon (with a wave vector k in the $\eta = \alpha, \beta$ for acoustic and optical branches, respectively) scattered to another magnon $\eta_{k'}'$ with different momentum by absorbing or emitting a phonon with wave vector q, the scattering rate by substituting $H_{\mathrm{c}}^{\mathrm{mp}}$ into Eq. (6) is expressed as

$$W_{\eta_k \to \eta_{k'}'}^{\mathrm{c}} = \frac{S_0}{4\pi m_{\mathrm{Cr}}} \sum_{\sigma} \int \frac{1}{\omega_{q\sigma}^{\mathrm{ph}}} \left[(N_{\eta_{k'}'} + 1)n_{q\sigma} \left| \Theta_{k,k',\sigma}^{\mathrm{c},\eta\eta'} \right|^2 \right.$$
$$\times \delta(\omega_{\eta_{k'}'} - \omega_{\eta_k} - \omega_{q\sigma}^{\mathrm{ph}})\delta_{k',k+q}$$
$$+ (N_{\eta_{k'}'} + 1)(n_{q\sigma} + 1)$$
$$\left. \times \left| \Theta_{k,k',\sigma}^{\mathrm{c},\eta\eta'} \right|^2 \delta(\omega_{\eta_{k'}'} - \omega_{\eta_k} + \omega_{q\sigma}^{\mathrm{ph}})\delta_{k',k-q} \right] dq, \quad (20)$$

with the first and second terms in the square bracket representing the phonon absorption and emission processes,
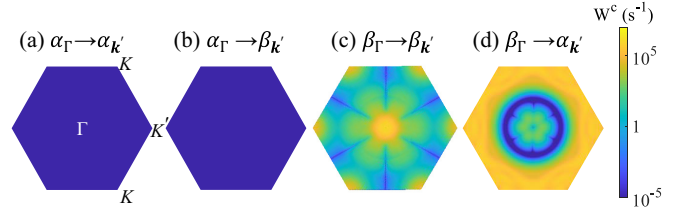
respectively. Here S_0 is the area of the unit cell and $N_{\eta_k}(n_{q\sigma})$ is the Planck distribution function for magnons (phonons). The total relaxation rate of a specific magnon state η_k then can be carried out through

$$W_{\eta_k}^{\mathrm{c}} = \sum_{k'} \sum_{\eta' = \alpha, \beta} W_{\eta_k \to \eta_{k'}'}^{\mathrm{c}}. \quad (21)$$

Unless otherwise specified, the temperature is taken to be 5 K in our numerical calculations and the (weak) temperature dependence is discussed in Sec. III C 4. Next, we consider the scattering processes from magnon states at some specific wave vectors.

1. Scattering from Γ magnon

The scattering rates from a magnon state at Γ point ($k = 0$) to other BZ points, i.e., $W_{\eta_k \to \eta_{k'}'}^{\mathrm{c}}$ in Eq. (20) with $\eta_k = \alpha_\Gamma$ (β_Γ) for the acoustic (optical) branch, are plotted in Fig. 4 by applying the Gaussian function for the δ function addressed in Eq. (7). Explicitly, we find, similar to the case in the three-dimensional case [49], all $W_{\alpha_\Gamma \to \eta_{k'}'}^{\mathrm{c}}$ vanish in Figs. 4(a) and 4(b). This can be seen from the expression of $\Theta_{k,k',\sigma}^{\mathrm{c},\kappa_1\kappa_2}$ by specifying $\kappa_1 = \alpha$ and $k = 0$, which leads to $B_k = -3(J_1 + J_3)S < 0$, therefore, $\mu_{\beta_\Gamma} = -\nu_{\beta_\Gamma} = -1/\sqrt{2}$ and $\gamma_1 = -h_1 = -1/\sqrt{2}$ according to Eqs. (13) and (19), respectively. The substitution of these relations into Eq. (18) immediately gives $\Theta_{\Gamma,k',\sigma}^{\mathrm{c},\alpha\kappa_2} = 0$.

For the intraband scatterings channel $\beta_\Gamma \to \beta_{k'}$, as shown in Fig. 4(c), the initial β_Γ magnons are most efficiently scattered to the nearby final states and those near K (K') point, by emitting or absorbing a low-energy acoustic phonon of a large occupation factor $n_{q\sigma}$. Large magnitude comes from nonzero coupling coefficient, i.e., $\Theta_{\Gamma,k',\sigma}^{\mathrm{c},\beta\kappa_2} \neq 0$, by substituting $\gamma_1 = h_2 = 1/\sqrt{2}$ into Eq. (18). The optical phonons do not contribute to $W_{\beta_\Gamma \to \beta_{k'}}^{\mathrm{c}}$ because their energies are all above the maximum value of the magnon energy transfer $\Delta E_1 = E_{\beta_\Gamma} - E_{\beta_K} = 4.14\,\mathrm{meV}$ for any possible intraband channels $\beta_\Gamma \to \beta_{k'}$.

The interband scattering rate $W_{\beta_\Gamma \to \alpha_{k'}}^{\mathrm{c}}$ in Fig. 4(d) shows a larger magnitude around the BZ boundary, where the energy transfer is relatively low. It is however worth pointing out that the phonon occupation factor $n_{q\sigma}$ is irrelevant to this feature, because only the emission of high-energy phonon ($\hbar\omega_{q\sigma}^{\mathrm{ph}} > \Delta E_1 \gg k_B T$) is allowed for this case, where we have $W_{\beta_\Gamma \to \alpha_{k'}}^{\mathrm{c}} \propto (1 + N_{\alpha_{k'}})(1 + n_{k'\sigma})|\Theta_{\Gamma,k',\sigma}^{\mathrm{c},\beta\alpha}|^2/\omega_{k'\sigma}^{\mathrm{ph}} \simeq (1 + N_{\alpha_{k'}})|\Theta_{\Gamma,k',\sigma}^{\mathrm{c},\beta\alpha}|^2/\omega_{k'\sigma}^{\mathrm{ph}}$. In particular, for those high-energy final magnon states $\alpha_{k'}$ far away from the BZ center, $N_{\alpha_{k'}} \ll 1$, so that the scattering rate is
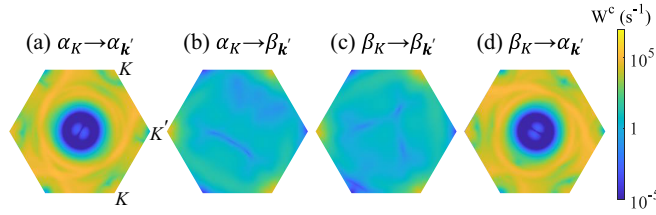
FIG. 5. The MNC scattering rates of different channels for an initial magnon at K point. The two degenerate K-magnon states are chosen as $\alpha_K = (a_K + b_K)/\sqrt{2}$ and $\beta_K = (a_K - b_K)/\sqrt{2}$.

FIG. 6. The MNC scattering rates $W^c_{\alpha_M \rightarrow \alpha_{k'}}$, $W^c_{\alpha_M \rightarrow \beta_{k'}}$, $W^c_{\beta_M \rightarrow \alpha_{k'}}$, and $W^c_{\beta_M \rightarrow \beta_{k'}}$ of a magnon state originally at M point.

mainly determined by the coupling coefficient $\Theta^{c,\beta\alpha}_{\Gamma,k',\sigma}$. For a detailed analysis we calculate the contribution of $W^c_{\beta_\Gamma \rightarrow \alpha_{k'}}$ from different phonon branches. The results from the phonon modes that contribute substantially, $\sigma = 4$, 5, and 11–14, are plotted as Fig. 13(a) in Appendix B, reflecting the essential role of these active phonon modes in Figs. 3(b) and 3(c). One may notice that there is a blue ring (inactive channels) in Fig. 4(d), which results from the forbidden transfer due to the phonon energy gap within 15–24 meV. For the final state at the BZ center, the scattering rate vanishes because $\Theta^{c,\beta\alpha}_{\Gamma,\Gamma,\sigma} = (\Theta^{c,\alpha\beta}_{\Gamma,\Gamma,\sigma})^* = 0$ as shown by the blue dot in the center in Fig. 4(d).

2. Scattering from K magnon

Figure 5 shows the scattering rates from the magnon state locating at one of the Dirac points (labeled as K). Since the acoustic and optical branches become degenerate at the Dirac points, the expressions of their wave functions $\alpha_K = (a_K + b_K e^{i\varphi})/\sqrt{2}$ and $\beta_K = (a_K - b_K e^{i\varphi})/\sqrt{2}$ contain an arbitrary factor φ, reflecting the nonunique description of (pseudo)spin orientation of the two degenerate eigenstates. The choice of φ, which specifies their (pseudo)spin orientations, is found to not affect much on the scattering rate (the scattering rates from α_K and β_K rely on the final states almost in the same way, except for a small difference in the inefficient channels to the final states around the BZ center). Results in Fig. 5 are calculated with $\varphi = 0$. A general feature for the four plots is that those final states nearby in the same K valley have large scattering rates, whereas the intervalley scatterings, i.e., from K valley to K' valley, are always forbidden. The latter is due to the lack of phonon satisfying simultaneously the energy and momentum conservations, more precisely, the lack of phonon with vanishing frequency but large wave vector.

The main difference between the scattering rates for the final states of α and β magnons, $\alpha_K(\beta_K) \rightarrow \alpha_{k'}$ and $\alpha_K(\beta_K) \rightarrow \beta_{k'}$, comes from the fact that the K point is the band minimum (maximum) of the optical (acoustic) magnon branch, hence only phonon absorption (emission) process can occur. The large energy transfer leads to a phonon occupation factor in the phonon absorption process $n_{q\sigma} \ll 1$ and that in the phonon emission process $1 + n_{q\sigma} \simeq 1$, therefore the scattering rate of $\alpha_K(\beta_K) \rightarrow \alpha_{k'}$, as shown in Figs. 5(a) and 5(d), associated with phonon emission could be much larger than that of $\alpha_K(\beta_K) \rightarrow \beta_{k'}$, as shown in Figs. 5(b) and 5(c), for k' far away from the K valley. The phonon-mode-resolved rate is plotted as Fig. 13(b) in Appendix B, which reveals that the brightest
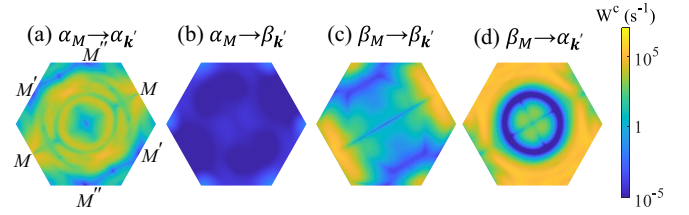
channels in $W^c_{\alpha_K \rightarrow \alpha_{k'}}$ and $W^c_{\beta_K \rightarrow \alpha_{k'}}$ are mostly contributed from $\sigma = 11$–14.

3. Scattering from M magnons

The scattering rate of a M magnon is plotted in Fig. 6. Similar to the K magnon case, the intraband scatterings $\alpha_M \rightarrow \alpha_{k'}$ and $\beta_M \rightarrow \beta_{k'}$, to different M' or M'' points, are forbidden. For the optical branch, the intraband scatterings, i.e., $\beta_M \rightarrow \beta_{k'}$, mainly scatter the M magnon to those final states along K-M-K' path as shown in Fig. 6(c), because the energy transfer from the β_M magnon to magnon states in other wave vector directions is too small to be matched by the energy of the emitted/absorbed phonon with the correct momentum transfer according to the conservation law. For the acoustic branch, the scattering rate of $\alpha_M \rightarrow \alpha_{k'}$ shows two active paths (two bright rings) as shown in Fig. 6(a). According to the phonon-mode-resolved analysis in Fig. 13(c), we find the two paths are activated by the phonons from $\sigma = 4$, 5 and $\sigma = 11$–14, respectively. Figure 13(c) also shows that the interband scattering from the optical branch to the acoustic one, $\beta_M \rightarrow \alpha_{k'}$, as shown in Fig. 6(d), is dominated by the phonon emission process with $\sigma = 11$–14. In contrast, the interband scatterings from the acoustic branch to the optical one, i.e., $\alpha_M \rightarrow \beta_{k'}$, are negligibly weak, as shown in Fig. 6 (b), because the population of the high-energy phonon (larger than $E_{\beta_K} - E_{\alpha_M} = 6.04$ meV) to be absorbed is rather small.

4. Magnon relaxation rate due to exchange-mediated magnon-phonon scatterings

By summing over the scattering rates to all possible final states, we calculate from Eq. (21) the magnon relaxation rates of the acoustic (α) and optical (β) magnons along the Γ-K-M-Γ path and plot them in Fig. 7(a) separately with blue and red curves. As one can see, the relaxation rate of β magnons can reach $10 \, \text{ns}^{-1}$ and that of α magnons is about one order of magnitude smaller around K point and becomes even much smaller approaching the Γ point. The dashed curves stand for the contributions from the optical phonons, i.e., the band index $\sigma = 4$–24. The nice agreement between the red dashed and solid curves again indicates the dominant role of the optical-phonon-involved processes for the relaxation of β magnons, because of their remarkable contribution to the interband scattering. Differently, the blue dashed curve differs significantly from the blue solid one, especially near Γ point as shown in the inset of Fig. 7(a), reflecting the importance of the acoustic phonon for the relaxation of α magnons. For the α magnons in the long wavelength regime ($k \lesssim 5 \times 10^8 \, \text{m}^{-1}$),
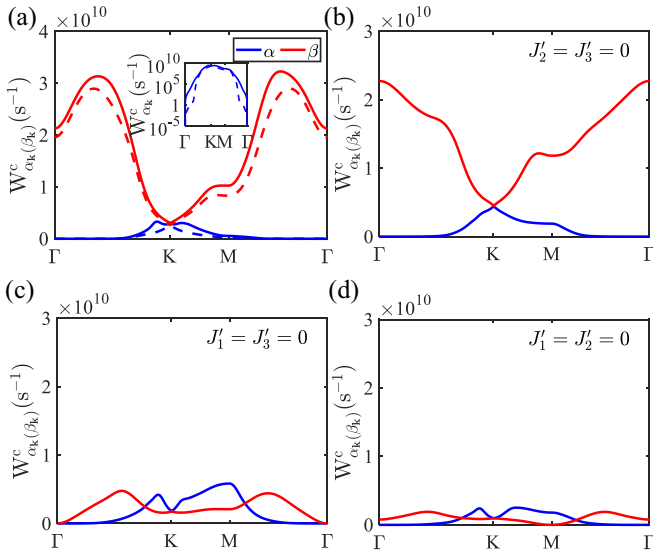
FIG. 7. (a) The total MNC scattering rates of the acoustic (blue solid curve) and optical (red solid curve) magnon states along the momentum path Γ-K-M-Γ. The dashed curves represent the contributions from optical phonons. The inset is a log scale plot for the total scattering rates of the α branch. (b)–(d) The scattering rates from the calculation with only the variation of the nearest-, next-nearest-, or the third-nearest-neighbor exchange interaction parameters taken into account.

$W^c_{\alpha_k}$ approximately follows k^2 dependence and vanishes at Γ point as shown in Fig. 14, similar to the three-dimensional case [49].

To examine the relative contribution of the different exchange variation terms, in Figs. 7(b)–7(d) we plot the results from the calculation with only one of the three parameters, J'_1, J'_2, or J'_3, taken into account. We find that the scattering of β mode is dominated by the nearest exchange parameter J'_1 in the long wavelength regime, while J'_2 and J'_3 contribute to its nonmonotonic behavior along the Γ-K and Γ-M paths. A similar nonmonotonic feature due to J'_2 and J'_3 also happens to the α mode. More interestingly, the total scattering rate in the short wavelength regime in Fig. 7(a), for instance at M point, is much smaller than the summation of the values from Figs. 7(b)–7(d), caused by the interference between three terms in Eq. (18). These features all suggest the importance of including the next-nearest- and the third-nearest-neighbor exchange interactions in the exchange-mediated magnon-phonon interaction.

The temperature dependence of the scattering rate from Γ and K magnons is shown in Fig. 8. As seen, the scatterings of the high-energy magnons β_Γ and α_K (β_K) are only slightly suppressed with decreasing temperature below 20 K, and tends to a saturated value at zero-temperature limit. This can be well understood from the factor $1 + n_{q\sigma} \to 1$ in the phonon emission limit. For α_Γ, $W^c_{\alpha_\Gamma}$ vanishes as explained in Sec. III C 1. We chose $k_0 = 0.9 \times 10^8$ m^{-1} close to Γ and calculate the temperature dependence of $W^c_{\alpha_{k_0}}$ as shown in the inset of Fig. 8. The factor $n_{q\sigma}$ of the phonon absorption leads to a strong dependence on the temperature.
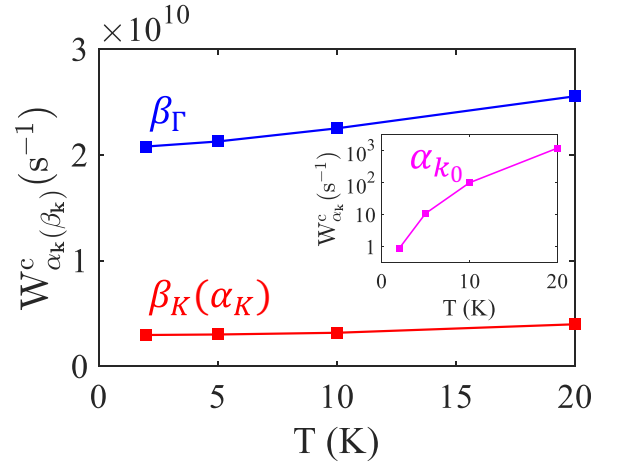
FIG. 8. Temperature dependence of MNC scattering rates for Γ and K magnons. Inset shows the scattering rates for $k_0 = 0.9 \times 10^8$ m^{-1} close to the Γ point as $W^c_{\alpha_\Gamma} = 0$.

IV. MNNC SCATTERING DUE TO ANISOTROPIC EXCHANGE INTERACTION IN CrI₃

So far, our calculations are based on the simplified model, where the spin exchange interaction is assumed to be in the Heisenberg form. Recent theoretical work shows that the exchange interaction in CrI$_3$ could go beyond the Heisenberg model with a weak anisotropic component between the nearest magnetic neighbors [90], owing to spin-orbit couplings [62]. Therefore, in this section we extend our calculation to analyze the consequence of such an anisotropic exchange term. As we will see, it introduces additional MNNC scatterings. Keep in mind that here we treat the anisotropy in a perturbative manner with its modification to magnon spectrum neglected. A nonperturbative treatment of such an anisotropic term will introduce a small magnon gap at K point [91], which has only negligible effects on the scattering rates we are interested in, because of its small magnitude compared to the isotropic part. The origin of the gap opening at K point in CrI$_3$ is an interesting but controversial issue, which has been comprehensively reviewed in Ref. [62].

A. Magnon-phonon interaction Hamiltonian due to the anisotropic exchange

The anisotropic exchange can be taken into account through a general exchange tensor [90], with which the spin-lattice coupling in Eq. (4) is replaced by

$$H^{\mathrm{mp}} = -\frac{1}{2}\sum_{i,j}[(\boldsymbol{X}_i - \boldsymbol{X}_j) \cdot \boldsymbol{d}_{ij}]\boldsymbol{S}_i \cdot \mathcal{J}'_{ij} \cdot \boldsymbol{S}_j. \quad (22)$$

After performing the standard quantization techniques and Fourier transformation, we derived the Hamiltonian of the magnon-phonon interaction. Since the anisotropy of the exchange tensor depends on the orientation of the Cr-Cr bond, specified to the nearest magnetic neighbors, the different Cr-Cr bonds can be connected through

$$\mathcal{J}'_{ii+\delta_2} = C_{3z}\mathcal{J}'_{ii+\delta_1}C_{3z}^{-1}, \quad \mathcal{J}'_{ii+\delta_3} = C_{3z}^2\mathcal{J}'_{ii+\delta_1}C_{3z}^{-2}, \quad (23)$$
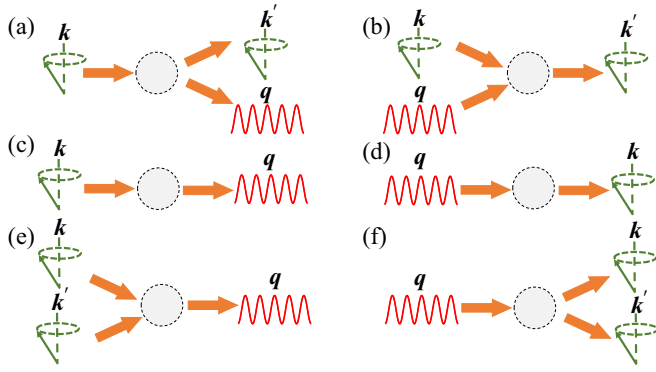
FIG. 9. Schematic diagrams of scattering processes between magnons (in green) and phonons (in red) with anisotropic exchange interaction. (a) and (b) The MNC processes for a magnon with momentum $\boldsymbol{k}$ scattered to be another magnon with $\boldsymbol{k}'$ by emitting or absorbing a phonon with momentum $\boldsymbol{q}$. (c) and (d) The interconversion processes from one magnon to one phonon, and vice versa. (e) and (f) The MNNC processes for two magnons with momentum $\boldsymbol{k}$ and $\boldsymbol{k}'$ merging into a single phonon with momentum $\boldsymbol{q}$ and its inverse process, respectively.

with $\boldsymbol{\delta}_i$ representing the three Cr-Cr bonds of the ith magnetic atom and C_{3z} (C_{3z}^2) corresponding to a 120° (240°) rotation around z axis. The magnon-phonon interaction thus can be expressed as

$$H^{\mathrm{mp}} = H_{\mathrm{c}}^{\mathrm{mp}} + H_{\mathrm{coup}}^{\mathrm{mp}} + H_{\mathrm{nc}}^{\mathrm{mp}}, \qquad (24)$$

where the first term $H_{\mathrm{c}}^{\mathrm{mp}}$ stands for the MNC term [see Figs. 9(a) and 9(b)] already fully included in Eq. (18) if we multiply the terms with $h^*\gamma$ (γ^*h) and h^*h ($\gamma^*\gamma$) thereby $[(\mathcal{J}_{ij}')^{xx} + (\mathcal{J}_{ij}')^{yy}]/(2J_{ij}')$ and $(\mathcal{J}_{ij}')^{zz}/J_{ij}'$, respectively. The second term in Eq. (24) is an interconversion term between one magnon and one phonon [see Figs. 9(c) and 9(d)] in the form of

$$H_{\mathrm{coup}}^{\mathrm{mp}} = \sum_{\boldsymbol{k},\sigma} \left(\Theta_{\boldsymbol{k},\sigma}^{\mathrm{coup},\alpha} \alpha_{\boldsymbol{k}} - \Theta_{\boldsymbol{k},\sigma}^{\mathrm{coup},\beta} \beta_{\boldsymbol{k}} \right) X_{\boldsymbol{k}\sigma} + \mathrm{H.c.}, \qquad (25)$$

which causes hybridization at the intersection points of the magnon and phonon dispersion curves and results in an anticrossing gap [62]. The coefficient in Eq. (25) is defined as

$$\Theta_{\boldsymbol{k},\sigma}^{\mathrm{coup},\kappa_1} = \frac{S\sqrt{2S}}{2} \sum_{\langle i,j \rangle} \frac{(\mathcal{J}_{ij}')^{xz} - i(\mathcal{J}_{ij}')^{yz}}{\mu_{\alpha_k} \nu_{\beta_k} - \nu_{\alpha_k} \mu_{\beta_k}}$$
$$\times (-h_{1,\boldsymbol{k}} + \gamma_{1,\boldsymbol{k}} e^{i\boldsymbol{k}\cdot\boldsymbol{R}_{ij}}) (e_{\mathrm{A},\boldsymbol{k}\sigma}^{ij} - e_{\mathrm{B},\boldsymbol{k}\sigma}^{ij} e^{-i\boldsymbol{k}\cdot\boldsymbol{R}_{ij}}). \qquad (26)$$

The last term in Eq. (24) is written as

$$H_{\mathrm{nc}}^{\mathrm{mp}} = \frac{1}{\sqrt{N}} \sum_{\boldsymbol{q},\boldsymbol{k},\sigma} \big[\Theta_{\boldsymbol{k},\boldsymbol{q}-\boldsymbol{k},\sigma}^{\mathrm{nc},\alpha\alpha} \alpha_{\boldsymbol{k}}^{\dagger} \alpha_{\boldsymbol{q}-\boldsymbol{k}}^{\dagger} - \Theta_{\boldsymbol{k},\boldsymbol{q}-\boldsymbol{k},\sigma}^{\mathrm{nc},\alpha\beta} \alpha_{\boldsymbol{k}}^{\dagger} \beta_{\boldsymbol{q}-\boldsymbol{k}}^{\dagger}$$
$$+ \Theta_{\boldsymbol{k},\boldsymbol{q}-\boldsymbol{k},\sigma}^{\mathrm{nc},\beta\beta} \beta_{\boldsymbol{k}}^{\dagger} \beta_{\boldsymbol{q}-\boldsymbol{k}}^{\dagger} - \Theta_{\boldsymbol{k},\boldsymbol{q}-\boldsymbol{k},\sigma}^{\mathrm{nc},\beta\alpha} \beta_{\boldsymbol{k}}^{\dagger} \alpha_{\boldsymbol{q}-\boldsymbol{k}}^{\dagger} \big] X_{\boldsymbol{q}\sigma} + \mathrm{H.c.}, \qquad (27)$$

which leads to the MNNC scattering processes with the creation (annihilation) of a magnon pair by annihilating (creating) a phonon [see Figs. 9(e) and 9(f)]. The coefficient in

Eq. (27) is defined as

$$\Theta_{\boldsymbol{k},\boldsymbol{k}',\sigma}^{\mathrm{nc},\kappa_1\kappa_2} = \sum_{\langle i,j \rangle} \frac{S[(\mathcal{J}_{ij}')^{xx} - (\mathcal{J}_{ij}')^{yy} + 2i(\mathcal{J}_{ij}')^{xy}]/2}{(\mu_{\alpha_k}^* \nu_{\beta_k}^* - \nu_{\alpha_k}^* \mu_{\beta_k}^*)(\nu_{\beta_{k'}}^* \mu_{\alpha_{k'}}^* - \nu_{\alpha_{k'}}^* \mu_{\beta_{k'}}^*)}$$
$$\times h_{1,\boldsymbol{k}'}^* \gamma_{2,\boldsymbol{k}'}^* (e_{\mathrm{A},\boldsymbol{k}+\boldsymbol{k}'\sigma}^{ij} e^{-i\boldsymbol{k}\cdot\boldsymbol{R}_{ij}} - e_{\mathrm{B},\boldsymbol{k}+\boldsymbol{k}'\sigma}^{ij} e^{i\boldsymbol{k}'\cdot\boldsymbol{R}_{ij}}), \qquad (28)$$

with $\gamma_{i,\boldsymbol{k}}$ and $h_{i,\boldsymbol{k}}$ being the same as those in Eq. (19).

B. MNNC scatterings

Next, we calculate the MNNC scattering rates from the interaction Hamiltonian (27). Focusing on the relaxation of an existing magnon, we consider the scattering process in Fig. 9(e), that is, an initial magnon with momentum $\boldsymbol{k}$ in α (β) branch gets scattered into a phonon $\boldsymbol{q}$ by absorbing another compensatory magnon $\boldsymbol{k}'$. The relaxation rate is given by

$$W_{\eta_k}^{\mathrm{nc}} = \sum_{\boldsymbol{k}'} \sum_{\eta'=\alpha,\beta} W_{\eta_k + \eta_{k'}' \to \mathrm{ph}}^{\mathrm{nc}}, \qquad (29)$$

where the rate of each scattering channel reads

$$W_{\eta_k + \eta_{k'}' \to \mathrm{ph}}^{\mathrm{nc}} = \frac{S_0}{4\pi m_{\mathrm{Cr}}} \sum_{\sigma} \int \frac{1}{\omega_{\boldsymbol{q}\sigma}^{\mathrm{ph}}} N_{\eta_{k'}'} (n_{\boldsymbol{q}\sigma} + 1) \delta_{\boldsymbol{k}+\boldsymbol{k}',\boldsymbol{q}}$$
$$\times \left| \Theta_{\boldsymbol{k},\boldsymbol{k}',\sigma}^{\mathrm{nc},\eta\eta'} \right|^2 \delta(\omega_{\boldsymbol{q}\sigma}^{\mathrm{ph}} - \omega_{\eta_{k'}'} - \omega_{\eta_k}) d\boldsymbol{q}. \qquad (30)$$

In order to calculate these MNNC scattering rates, one needs the values of the matrix elements, $(\mathcal{J}_{ij}')^{xx}$, $(\mathcal{J}_{ij}')^{yy}$, and $(\mathcal{J}_{ij}')^{xy}$, according to Eq. (28). Those are in principle accessible from the first-principles calculations. The precise determination of these parameters, on one hand, is quite challenging, and there is no reported data in the literature. On the other hand, the explicit values of these parameters apparently only introduce a modification upon all scattering rates by an overall prefactor without any change in the detailed behavior. Therefore, in this part, we do not perform explicit calculation for these parameters but estimate them with a naive assumption $(\mathcal{J}_{ij}')^{mn} \propto \mathcal{J}_1^{mn}$. In Ref. [90] the exchange parameters between the nearest neighbors are reported as $\mathcal{J}_{ii+\delta_1}^{xx} = 2.29\,\mathrm{meV}$, $\mathcal{J}_{ii+\delta_1}^{yy} = 1.93\,\mathrm{meV}$, $\mathcal{J}_{ii+\delta_1}^{zz} = 2.23\,\mathrm{meV}$, and $\mathcal{J}_{ii+\delta_1}^{xy} = -0.3\,\mathrm{meV}$, which suggest that the anisotropic elements $\mathcal{J}_{ii+\delta_1}^{xx} - \mathcal{J}_{ii+\delta_1}^{yy}$ and $\mathcal{J}_{ii+\delta_1}^{xy}$ are around one order of magnitude smaller than the isotropic part $\bar{J}_1 \sim (\mathcal{J}_{ii+\delta_1}^{xx} + \mathcal{J}_{ii+\delta_1}^{yy} + \mathcal{J}_{ii+\delta_1}^{zz})/3$. In addition, one may think about the magnetic dipole-dipole interaction, which also varies with the distance between magnetic atoms, and hence gives a similar MNNC magnon-phonon scattering due to its anisotropic exchange-type form

$$H_{\mathrm{DDI}} = \frac{\mu_0(g\mu_B)^2}{2} \sum_{i \neq j} \frac{(\boldsymbol{S}_i \cdot \boldsymbol{S}_j) - 3(\boldsymbol{d}_{ij} \cdot \boldsymbol{S}_i)(\boldsymbol{d}_{ij} \cdot \boldsymbol{S}_j)}{r_{ij}^3}. \qquad (31)$$

For example, from its derivative with respect to the distance, one can estimate its contribution to the effective parameter between the nearest neighbors

$$(\mathcal{J}_{\mathrm{DDI}}')^{xy} = \frac{3\sqrt{3}}{4} \bar{J}_{\mathrm{DDI}} \approx -0.04\,\mathrm{meV/\mathring{A}}, \qquad (32)$$

which is also around one order of magnitude smaller than J_1'. With this consideration, in the following calculation we adopt $(\mathcal{J}_{ii+\delta_1}')^{xx} - (\mathcal{J}_{ii+\delta_1}')^{yy} \approx (\mathcal{J}_{ii+\delta_1}')^{xy} \approx 0.1J_1' \approx 0.15\,\mathrm{meV/\mathring{A}}$.
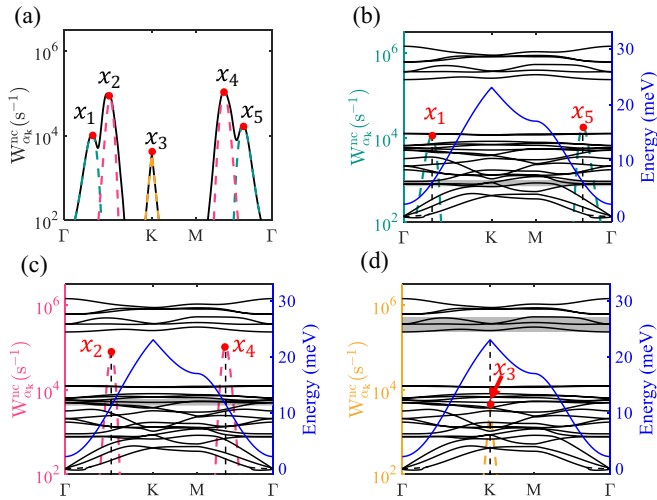
FIG. 10. (a) The total MNNC scattering rates $W_{\alpha_k}^{\text{nc}}$ (black solid curve) and the contributions from the selected phonon modes $\sigma = 4$–6 (green-dashed curve), $\sigma = 11$–14 (pink-dashed curve), and $\sigma = 19$–21 (yellow-dashed curve) along the closed path Γ-K-M-Γ. (b)–(d) Replot the dashed curves in (a) together with the phonon spectrum and the threshold of the phonon energy for two-magnon annihilation process (blue curve) $\hbar\omega_{\text{th}} = \hbar\omega_{\alpha_k} + \hbar\omega_{\alpha_\Gamma}$, which shows a nice agreement between the peaks of the dashed curves and the intersections between the selected phonon bands (shadowed window) and threshold energy.

The relaxation rates of the α_k and β_k magnon are plotted in Figs. 10(a) and 11(a), respectively, both of which show rich momentum dependence. The scattering rates due to specific phonon modes (mainly those active phonon modes shown in Fig. 3) are plotted with dashed curves in the same figures, which reveal that the behavior of the relaxation rate originates from the interplay of different scattering channels. The resonancelike shape of each channel can be well understood from the magnon and phonon spectra, as discussed below. Before that, we would like to point out that when an initial magnon is scattered to become a phonon with a compensatory magnon at $\alpha_{k'}$ or $\beta_{k'}$ state, the scattering rate satisfies $W_{\eta_k + \beta_{k'} \rightarrow \text{ph}}^{\text{nc}} \ll W_{\eta_k + \alpha_{k'} \rightarrow \text{ph}}^{\text{nc}}$ because $N_{\beta_{k'}} \ll N_{\alpha_{k'}}$ is determined by their energy. So the contribution of $W_{\eta_k + \beta_{k'} \rightarrow \text{ph}}^{\text{nc}}$ to $W_{\eta_k}^{\text{nc}}$ is neglected in the following analysis.

Specifically, the contribution to the α_k magnon scattering via the selected channels (with the small phonon energy window covering the 4–6 phonon modes highlighted with gray) is plotted as a green dashed curve in Fig. 10(b). The blue curve stands for the energy threshold of the emitted phonon from the α_k magnon state, i.e., $\hbar\omega_{\text{th}} = \hbar\omega_{\alpha_k} + \hbar\omega_{\alpha_\Gamma}$. The positions of the peaks (labeled as x_1 and x_5) in the scattering rates show good agreement with intersection points between the threshold curve and the phonon dispersion curves of the selected modes. In the region where the energy of the selected phonon is far below the threshold, i.e., $\hbar\omega_{q\sigma}^{\text{ph}} \ll \hbar\omega_{\text{th}}$, the MNNC process is forbidden, reflected by the rather negligible rate in the figure. This also indicates that the acoustic phonons are all irrelevant to the MNNC scatterings. In the opposite limit with $\hbar\omega_{q\sigma}^{\text{ph}} \gg \hbar\omega_{\text{th}}$, the energy of the compensatory magnon is too high to give a notable $N_{\alpha_{k'}}$ appearing in Eq. (30). As a result,
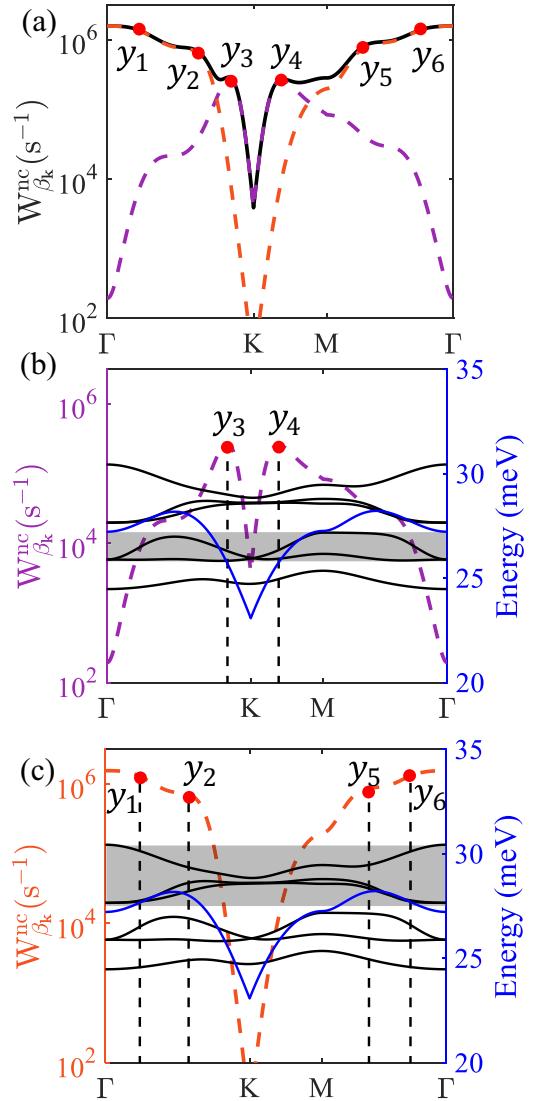
FIG. 11. (a) The MNNC scattering rates $W_{\beta_k}^{\text{nc}}$ (black solid curve) with the dashed curves representing the contribution from selected phonon branches $\sigma = 20$ and 21 [shadowed window in (b)] and $\sigma = 22$–24 [shadowed window in (c)]. The blue curve in (b) and (c) stands for the threshold of the phonon energy $\hbar\omega_{\text{th}} = \hbar\omega_{\beta_k} + \hbar\omega_{\alpha_\Gamma}$ for the corresponding annihilation of the β_k magnon.

a resonancelike peak shows up at $\hbar\omega_{q\sigma}^{\text{ph}} \sim \hbar\omega_{\text{th}}$. Similarly, as shown in Fig. 10(c), the intersection points between the threshold curve and the phonon energy window covering the 11–14 modes fit well with the peaks indicated as x_2 and x_4. On the other hand, for the high-energy optical phonons overall above the threshold curve, as shown in Fig. 10(d), the maximal scattering rate is achieved at the K point with the minimum energy of the compensatory magnon $\alpha_{k'}$ and hence maximal $N_{\alpha_{k'}}$ leading to the peak x_3.

For the initial magnon at β_k state, all scattering processes associated with another $\beta_{k'}$ are forbidden because any combination energy $\hbar\omega_{\beta_k} + \hbar\omega_{\beta_{k'}}$ is above all phonon energies. The threshold for this MNNC process is then given by $\hbar\omega_{\beta_k} + \hbar\omega_{\alpha_\Gamma}$, as indicated by the blue curves in Figs. 11(b) and

11(c), only the high-frequency branches ($\sigma = 20$–24) above the phonon band gap are relevant. Similar to the previous α_k case, the interaction between the threshold curve and the active phonon modes results in maximums ($y_1 - y_6$) in the scattering rates. The interplay between the contributions from different scattering channels again leads to the nonmonotonic momentum dependence in the total relaxation rates.

V. CONCLUSION AND DISCUSSION

In summary, we derived the magnon-phonon interaction due to the variation of the exchange strengths, up to the third-nearest-neighbor interaction, introduced by the lattice vibration. We applied the formalism, combined with first-principles calculations, to monolayer CrI$_3$ and computed the magnon-phonon scattering rates therein. Beyond the widely used long-wavelength approximation, we employed the precise magnon and phonon spectra, as well as the corresponding wave functions, from first-principles calculation, and achieved quantitative evaluation of the scattering rates in the entire Brillouin zone. We further analyzed the relative contribution from different phonon modes, not only the acoustic branches but also optical ones. Specifically, we presented the detailed analysis of the scattering channels for an initial Γ-, K-, or M-magnon, where the scattering by a phonon associated with a relatively large in-plane atomic vibration is mostly relevant. The total scattering rate to all possible final states was found to be able to reach $10\,\mathrm{ns}^{-1}$, where the second- and third-nearest-neighbor contributions remain relevant. The scattering rate of the acoustic magnon in the long wavelength regime shows quadratic dependence on the wave vector and vanishes at Γ point, which can also be well understood from our analytical expression of the magnon-phonon interaction strength. The extension to the anisotropic exchange term activates the magnon-number-nonconserving scattering channels. The detailed calculation of the processes with two magnons merging into a phonon shows rich nonmonotonic behaviors in the momentum dependence of the scattering rates, which can be well explained by the large in-plane atomic vibration of the associated phonon. Our results reveal the important role of the optical phonons in magnon relaxation, and our first-principles-based approach provides a good solution to quantitatively evaluate the magnon relaxation due to magnon-phonon interaction and perhaps other magnetic interactions, such as the dynamical Dzyaloshinskii-Moriya interaction due to the out-of-plane vibration [92].

ACKNOWLEDGMENTS

APPENDIX A: EXCHANGE PARAMETERS FROM FIRST-PRINCIPLES CALCULATION

The three Heisenberg exchange parameters from the first-principles approach addressed in Sec. III A are plotted as filled dots in Fig. 12 as a function of lattice constant a. For each a value, the lattice is fully relaxed until the residual interatomic
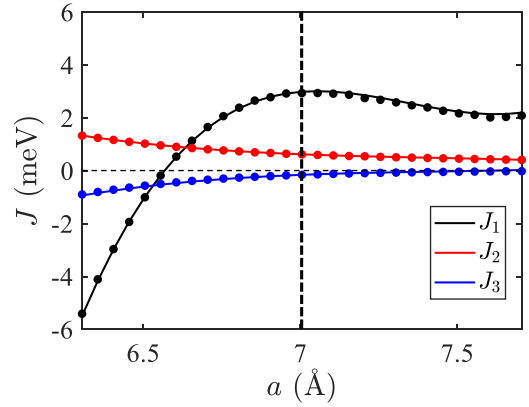
FIG. 12. The values of the nearest- (J_1), next-nearest- (J_2), and third-nearest-neighbor (J_3) exchange parameters as a function of the lattice constant a. Symbols are calculated results with error bars smaller than symbol size. Solid curves are a numerical fit. The vertical dashed line indicates the equilibrium lattice constant $a_0 = 7.005\,\text{Å}$.

forces are below 0.01 eV/Å. We fit the exchange parameters as

$$J_1 = 9.448a^3 - 208a^2 + 1524.0955a - 3714.35,$$

$$J_2 = -0.3945a^3 + 8.798a^2 - 65.645a + 164.35,$$

$$J_3 = 0.4512a^3 - 10.09a^2 + 75.406a - 188.35,$$

shown by the solid curves in Fig. 12. From the derivative with respect to lattice constant a, we obtain the magnon-phonon coupling parameters as

$$J'_{1(2,3)} = \frac{\partial_a J_{1(2,3)}|_{a=a_0}}{\partial_a d_{1(2,3)}}, \qquad (\text{A1})$$

where a_0 is the equilibrium lattice constant. The distances of the three types of exchange pairs read $d_1 = d_2/\sqrt{3} = d_3/2 = a/\sqrt{3}$.
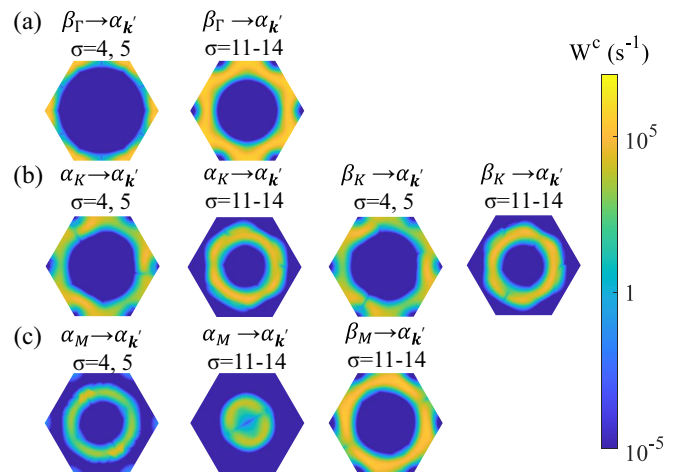
FIG. 13. The MNC scattering rates associated with the selected phonons modes for an initial magnon at (a) Γ, (b) K, and (c) M points, respectively.
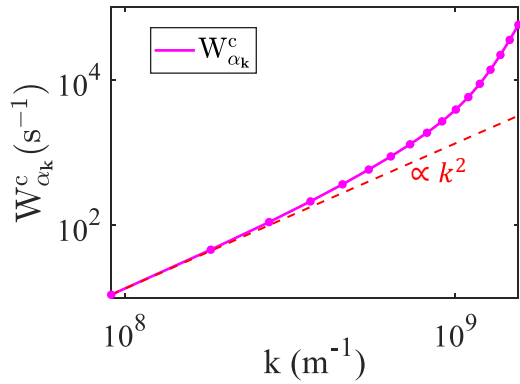
FIG. 14. The relaxation rate of α magnon due to MNC scattering $W_{\alpha_k}^c$ and the fitted result with $\sim k^2$ (red line) in the long-wavelength region ($k \lesssim 5 \times 10^8$ m^{-1}).

APPENDIX B: MNC SCATTERING RATES DUE TO DIFFERENT OPTICAL PHONONS

According to the analysis in the main text, the MNC scatterings mainly result from the optical phonons with atomic relative vibrations in x-y plane, i.e., the phonon modes $\sigma = 4$, 5, and 11–14 shown in Figs. 3(b) and 3(c). The contributions of selected phonon modes to the intraband or interband scatterings from an initial magnon state at Γ, K, or M point are plotted in Fig. 13, whose detailed description is given in Sec. III C.

APPENDIX C: SCATTERING RATE OF ACOUSTIC MAGNONS IN THE LONG-WAVELENGTH REGION

The total scattering rate of acoustic magnons, $W_{\alpha_k}^c$, calculated from Eq. (21), is plotted as the pink solid curve in Fig. 14, where the red dashed one indicates the fitting with k^2. To understand this relation we expand $\Theta_{k,k',\sigma}^{c,\alpha\kappa_2}$ in Eq. (18), with respect to k. As explained in Sec. III C 1, $\Theta_{k,k',\sigma}^{c,\alpha\kappa_2} = 0$ for $k = 0$, indicating the vanishing of the zero order. Therefore, the lowest nonzero term could be linear in k, which can be easily seen, for example, from the last term in Eq. (18)

$$\sin[(k'-k)\cdot R_{ij}] + \sin(k \cdot R_{ij}) - \sin(k' \cdot R_{ij})$$
$$\approx (k \cdot R_{ij})[1 - \cos(k' \cdot R_{ij})].$$

The quadratic dependence then manifests itself from Eq. (20).

[1] M. P. Kostylev, A. A. Serga, T. Schneider, B. Leven, and B. Hillebrands, Appl. Phys. Lett. **87**, 153501 (2005).

[2] T. Schneider, A. A. Serga, B. Leven, B. Hillebrands, R. L. Stamps, and M. P. Kostylev, Appl. Phys. Lett. **92**, 022505 (2008).

[3] M. Jamali, J. H. Kwon, S.-M. Seo, K.-J. Lee, and H. Yang, Sci. Rep. **3**, 3160 (2013).

[4] S. Klingler, P. Pirro, T. Brächer, B. Leven, B. Hillebrands, and A. V. Chumak, Appl. Phys. Lett. **105**, 152410 (2014).

[5] A. A. Nikitin, A. B. Ustinov, A. A. Semenov, A. V. Chumak, A. A. Serga, V. I. Vasyuchka, E. Lähderanta, B. A. Kalinikos, and B. Hillebrands, Appl. Phys. Lett. **106**, 102405 (2015).

[6] A. B. Ustinov, E. Lähderanta, M. Inoue, and B. A. Kalinikos, IEEE Magn. Lett. **10**, 1 (2019).

[7] Q. Wang, M. Kewenig, M. Schneider, R. Verba, F. Kohl, B. Heinz, M. Geilen, M. Mohseni, B. Lägel, F. Ciubotaru, C. Adelmann, C. Dubs, S. D. Cotofana, O. V. Dobrovolskiy, T. Brächer, P. Pirro, and A. V. Chumak, Nat. Electron. **3**, 765 (2020).

[8] G. Csaba, A. Papp, and W. Porod, Phys. Lett. A **381**, 1471 (2017).

[9] A. Mahmoud, F. Ciubotaru, F. Vanderveken, A. V. Chumak, S. Hamdioui, C. Adelmann, and S. Cotofana, J. Appl. Phys. **128**, 161101 (2020).

[10] A. V. Chumak, P. Kabos, M. Wu, C. Abert, C. Adelmann, A. O. Adeyeye, J. Åkerman, F. G. Aliev, A. Anane, A. Awad et al., IEEE Trans. Magn. **58**, 1 (2022).

[11] S. A. Wolf, D. D. Awschalom, R. A. Buhrman, J. M. Daughton, S. von Molnár, M. L. Roukes, A. Y. Chtchelkanova, and D. M. Treger, Science **294**, 1488 (2001).

[12] A. Soumyanarayanan, N. Reyren, A. Fert, and C. Panagopoulos, Nature (London) **539**, 509 (2016).

[13] R. Khymyn, I. Lisenkov, V. Tiberkevich, B. A. Ivanov, and A. Slavin, Sci. Rep. **7**, 43705 (2017).

[14] O. Sulymenko, O. Prokopenko, I. Lisenkov, J. Åkerman, V. Tyberkevych, A. N. Slavin, and R. Khymyn, J. Appl. Phys. **124**, 152115 (2018).

[15] V. Baltz, A. Manchon, M. Tsoi, T. Moriyama, T. Ono, and Y. Tserkovnyak, Rev. Mod. Phys. **90**, 015005 (2018).

[16] R. Khymyn, I. Lisenkov, J. Voorheis, O. Sulymenko, O. Prokopenko, V. Tiberkevich, J. Akerman, and A. Slavin, Sci. Rep. **8**, 15727 (2018).

[17] A. V. Chumak, A. A. Serga, and B. Hillebrands, Nat. Commun. **5**, 4700 (2014).

[18] A. V. Chumak, V. I. Vasyuchka, A. A. Serga, and B. Hillebrands, Nat. Phys. **11**, 453 (2015).

[19] P. W. Anderson, Phys. Rev. **109**, 1492 (1958).

[20] R. M. Toussaint, D. W. Hone, V. Jaccarino, and S. M. Rezende, Phys. Rev. B **30**, 3859 (1984).

[21] W. Brenig and A. P. Kampf, Phys. Rev. B **43**, 12914 (1991).

[22] M. Oogane, T. Wakitani, S. Yakata, R. Yilgin, Y. Ando, A. Sakuma, and T. Miyazaki, Jpn. J. Appl. Phys. **45**, 3889 (2006).

[23] C. Scheck, L. Cheng, I. Barsukov, Z. Frait, and W. E. Bailey, Phys. Rev. Lett. **98**, 117601 (2007).

[24] W. Brenig and A. L. Chernyshev, Phys. Rev. Lett. **110**, 157203 (2013).

[25] E. Abrahams and C. Kittel, Phys. Rev. **88**, 1200 (1952).

[26] C. Kittel and E. Abrahams, Rev. Mod. Phys. **25**, 233 (1953).

[27] N. Bloembergen and S. Wang, Phys. Rev. **93**, 72 (1954).

[28] C. Kittel, Phys. Rev. **110**, 836 (1958).

[29] M. I. Kaganov and V. M. Tsukernik, Sov. Phys. JETP **9**, 151 (1959).

[30] A. G. Gurevich and G. A. Melkov, *Magnetization Oscillations and Waves*, 1st ed. (CRC, Boca Raton, FL, 1996).

[31] P. Dai, H. Y. Hwang, J. Zhang, J. A. Fernandez-Baca, S.-W. Cheong, C. Kloc, Y. Tomioka, and Y. Tokura, Phys. Rev. B **61**, 9553 (2000).

[32] M. Sparks, R. Loudon, and C. Kittel, Phys. Rev. **122**, 791 (1961).

[33] D. L. Huber, Phys. Rev. **136**, A500 (1964).

[34] A. B. Harris, D. Kumar, B. I. Halperin, and P. C. Hohenberg, Phys. Rev. B **3**, 961 (1971).

[35] S. P. Bayrakci, D. A. Tennant, P. Leininger, T. Keller, M. C. R. Gibson, S. D. Wilson, R. J. Birgeneau, and B. Keimer, Phys. Rev. Lett. **111**, 017204 (2013).

[36] K. Shen, Phys. Rev. Lett. **124**, 077201 (2020).

[37] K. Wang, X. Xu, Y. Cheng, M. Zhang, J. S. Wang, H. Wang, and G. Zhang, Phys. Rev. B **102**, 235434 (2020).

[38] L. Berger, Phys. Rev. B **54**, 9353 (1996).

[39] Y. Tserkovnyak, A. Brataas, and G. E. W. Bauer, Phys. Rev. Lett. **88**, 117601 (2002).

[40] E. Carpene, E. Mancini, C. Dallera, M. Brenna, E. Puppin, and S. De Silvestri, Phys. Rev. B **78**, 174422 (2008).

[41] M. Haag, C. Illg, and M. Fähnle, Phys. Rev. B **90**, 014417 (2014).

[42] M. C. T. D. Müller, S. Blügel, and C. Friedrich, Phys. Rev. B **100**, 045130 (2019).

[43] R. F. Sabiryanov and S. S. Jaswal, Phys. Rev. Lett. **83**, 2062 (1999).

[44] L. M. Woods, Phys. Rev. B **65**, 014409 (2001).

[45] A. I. Bezuglyj, V. A. Shklovskij, V. V. Kruglyak, and R. V. Vovk, Phys. Rev. B **100**, 214409 (2019).

[46] A. Rückriegel, P. Kopietz, D. A. Bozhko, A. A. Serga, and B. Hillebrands, Phys. Rev. B **89**, 184413 (2014).

[47] Y. Liu, L.-S. Xie, Z. Yuan, and K. Xia, Phys. Rev. B **96**, 174416 (2017).

[48] S. F. Maehrlein, I. Radu, P. Maldonado, A. Paarmann, M. Gensch, A. M. Kalashnikova, R. V. Pisarev, M. Wolf, P. M. Oppeneer, J. Barker, and T. Kampfrath, Sci. Adv. **4**, eaar5164 (2018).

[49] S. Streib, N. Vidal-Silva, K. Shen, and G. E. W. Bauer, Phys. Rev. B **99**, 184442 (2019).

[50] L.-W. Wang, L.-S. Xie, P.-X. Xu, and K. Xia, Phys. Rev. B **101**, 165137 (2020).

[51] G. Laurence and D. Petitgrand, Phys. Rev. B **8**, 2130 (1973).

[52] A. V. Kimel, R. V. Pisarev, J. Hohlfeld, and T. Rasing, Phys. Rev. Lett. **89**, 287401 (2002).

[53] K. Wang, J. He, M. Zhang, H. Wang, and G. Zhang, Nanotechnology **31**, 435705 (2020).

[54] K.-M. Ho, C. L. Fu, B. N. Harmon, W. Weber, and D. R. Hamann, Phys. Rev. Lett. **49**, 673 (1982).

[55] S. V. Halilov, A. Y. Perlov, P. M. Oppeneer, and H. Eschrig, Europhys. Lett. **39**, 91 (1997).

[56] S. V. Halilov, H. Eschrig, A. Y. Perlov, and P. M. Oppeneer, Phys. Rev. B **58**, 293 (1998).

[57] Y. Liu, Z. Yuan, R. J. H. Wesselink, A. A. Starikov, M. van Schilfgaarde, and P. J. Kelly, Phys. Rev. B **91**, 220405(R) (2015).

[58] M. Aßmann and U. Nowak, J. Magn. Magn. Mater. **469**, 217 (2019).

[59] M. Strungaru, M. O. A. Ellis, S. Ruta, O. Chubykalo-Fesenko, R. F. L. Evans, and R. W. Chantrell, Phys. Rev. B **103**, 024429 (2021).

[60] J. Barker and G. E. W. Bauer, Phys. Rev. Lett. **117**, 217201 (2016).

[61] M. Weißenhofer, L. Rózsa, and U. Nowak, Phys. Rev. Lett. **127**, 047203 (2021).

[62] P. Delugas, O. Baseggio, I. Timrov, S. Baroni, and T. Gorni, arXiv:2105.04531.

[63] B. Huang, G. Clark, E. Navarro-Moratalla, D. R. Klein, R. Cheng, K. L. Seyler, D. Zhong, E. Schmidgall, M. A. McGuire, D. H. Cobden, W. Yao, D. Xiao, P. Jarillo-Herrero, and X. Xu, Nature (London) **546**, 270 (2017).

[64] T. Holstein and H. Primakoff, Phys. Rev. **58**, 1098 (1940).

[65] P. Giannozzi, S. Baroni, N. Bonini, M. Calandra, R. Car, C. Cavazzoni, D. Ceresoli, G. L. Chiarotti, M. Cococcioni, I. Dabo et al., J. Phys.: Condens. Matter **21**, 395502 (2009).

[66] P. Giannozzi, O. Andreussi, T. Brumme, O. Bunau, M. B. Nardelli, M. Calandra, R. Car, C. Cavazzoni, D. Ceresoli, M. Cococcioni et al., J. Phys.: Condens. Matter **29**, 465901 (2017).

[67] K. Shen, New J. Phys. **20**, 043025 (2018).

[68] S. S. Pershoguba, S. Banerjee, J. C. Lashley, J. Park, H. Ågren, G. Aeppli, and A. V. Balatsky, Phys. Rev. X **8**, 011010 (2018).

[69] J. Liu, L. Wang, and K. Shen, Phys. Rev. B **102**, 144416 (2020).

[70] G. Kresse and J. Hafner, Phys. Rev. B **47**, 558 (1993).

[71] G. Kresse and J. Furthmüller, Phys. Rev. B **54**, 11169 (1996).

[72] J. P. Perdew, K. Burke, and M. Ernzerhof, Phys. Rev. Lett. **77**, 3865 (1996).

[73] G. Kresse and D. Joubert, Phys. Rev. B **59**, 1758 (1999).

[74] P. E. Blöchl, Phys. Rev. B **50**, 17953 (1994).

[75] H. J. Monkhorst and J. D. Pack, Phys. Rev. B **13**, 5188 (1976).

[76] L. Webster and J.-A. Yan, Phys. Rev. B **98**, 144411 (2018).

[77] H. Wang, F. Fan, S. Zhu, and H. Wu, Europhys. Lett. **114**, 47001 (2016).

[78] W.-B. Zhang, Q. Qu, P. Zhu, and C.-H. Lam, J. Mater. Chem. C **3**, 12457 (2015).

[79] F. Zheng, J. Zhao, Z. Liu, M. Li, M. Zhou, S. Zhang, and P. Zhang, Nanoscale **10**, 14298 (2018).

[80] L. Chen, J.-H. Chung, B. Gao, T. Chen, M. B. Stone, A. I. Kolesnikov, Q. Huang, and P. Dai, Phys. Rev. X **8**, 041028 (2018).

[81] S. Baroni, P. Giannozzi, and A. Testa, Phys. Rev. Lett. **58**, 1861 (1987).

[82] S. Baroni, S. de Gironcoli, A. dal Corso, and P. Giannozzi, Rev. Mod. Phys. **73**, 515 (2001).

[83] L. Webster, L. Liang, and J.-A. Yan, Phys. Chem. Chem. Phys. **20**, 23546 (2018).

[84] C.-C. Lee, C.-E. Hsu, and H.-C. Hsueh, J. Phys.: Condens. Matter **33**, 055902 (2020).

[85] F. Kargar, E. A. Coleman, S. Ghosh, J. Lee, M. J. Gomez, Y. Liu, A. S. Magana, Z. Barani, A. Mohammadzadeh, B. Debnath, R. B. Wilson, R. K. Lake, and A. A. Balandin, ACS Nano **14**, 2424 (2020).

[86] H. Zabel, J. Phys.: Condens. Matter **13**, 7679 (2001).

[87] T. Kühn, D. V. Anghel, J. P. Pekola, M. Manninen, and Y. M. Galperin, Phys. Rev. B **70**, 125425 (2004).

[88] C. Lin, S. Poncé, and N. Marzari, npj Comput. Mater. **8**, 236 (2022).

[89] B. Sadhukhan, A. Bergman, Y. O. Kvashnin, J. Hellsvik, and A. Delin, Phys. Rev. B **105**, 104418 (2022).

[90] C. Xu, J. Feng, H. Xiang, and L. Bellaiche, npj Comput. Mater. **4**, 57 (2018).

[91] E. Aguilera, R. Jaeschke-Ubiergo, N. Vidal-Silva, L. E. F. F. Torres, and A. S. Nunez, Phys. Rev. B **102**, 024409 (2020).

[92] K. Shen, Phys. Rev. B **106**, 104411 (2022).